# Analysis of the instability conditions and failure mode of a special type of translational landslide using long-term monitoring data: A case study of the Wobaoshi landslide (in Bazhong, China)

Yimin Liu[a,b], Chenghu Wang[a,*], Guiyun Gao[a], Pu Wang[a], Zhengyang Hou[a], Qisong Jiao[a]

[a] Institute of Crustal Dynamics, China Earthquake Administration, Beijing, 100085, China

[b] School of Manufacturing Science & Engineering, Sichuan University, Chengdu, 611730 ,*China*

**Abstract:** A translational landslide comprising nearly horizontal sandstone and mudstone interbed occurred in the Ba river basin of the Qinba–Longnan mountain area. Previous studies have succeeded to some extent in investigating on the formation mechanism and failure mode of this type of rainfall-induced landslide; however, it is very difficult to demonstrate and validate the previously-established geomechanial model owing to lack of landslide monitoring data. In this study, we considered a translational landslide exhibiting an unusual morphology, ie., the Wobaoshi landslide, that occurred in Bazhong, China. First, the engineering geological conditions of this landslide were determined through field investigation, and the deformation and failure mode of the plate-shaped main body were analyzed. Second, long-term monitoring was performed to obtain multiparameter monitoring data (width of the crown crack, rainfall, and pore-water pressure). Finally, an equation was developed to obtain the critical water height of the multistage bodies, i.e., $h_{cr}$, based on the geomechanical model analysis of the multistage main bodies, and the reliability of this equation was verified using long-term monitoring data. Subsequently, the deformation and failure modes of the plate-shaped bodies were analyzed and investigated based on numerical simulations and calculations. Thus, the multiparameter monitoring data proved that the stability of

the main body is majorly controlled by the rainfall and pore-water pressure, further, the pore-water pressure in the crown crack was positive with respect to the initiation of sliding of the plate-shaped bodies. Simultaneously, an optimized monitoring methodology was proposed for this type of landslide. Therefore, these research findings are theoretically and practically significant to study the translational landslides occurring in this area.

**Keywords:** Translational landslide; Long- term monitoring; Instability conditions; Failure mode; Plate-shaped main body; Pore-water pressure.

# 0. Introduction

A special type of landslide can be observed in the red beds of the Qinba–Longnan mountainous area. This landslide mainly occurres in the rock mass of the nearly horizontal sandstone and mudstone interbed located in the Ba river basin, and hasexhibits the following characteristics: The cover layer is ~~extremely~~ thin (generally not more than 5 m); the sliding surface is nearly horizontal; and the inclination angle of the rock bed is generally only $3^{\circ} \sim 8^{\circ}$. The main body of this landslide is typically a thick sandstone layer with good integrity, whereas its bottom is a weak layer comprising mudstone. During monsoon, particularly during rainstorms, the main body is pushed horizontally along the sliding surface. Some scholars have termed this phenomenon a flat-push landslide, which is a typical rainfall-induced landslide (Zhang et al., 1994; Guzzetti et al., 2004; Xu et al., 2010).

The research on the formation mechanism and deformation mode of a translational landslide is mainly classified into two categories. The first category includes the translational landslides that are primarily caused by the hydrostatic pressure or confined water pressure because of rainstorms

(Kong and Chen, 1989; Matjaž et al., 2004; Yin et al., 2005). The main body of the thick sandstone can slide along the surface owing to the hybrid action of the hydrostatic pressure in crown cracks and the uplift force of the sliding surface (Wang and Zhang, 1985; Zhang et al., 1994; Xu et al., 2006; Fan, 2007). Simultaneously, the sliding soil, which is expanded by rainwater, causes a slip between the nearly horizontal layers (Yin et al., 2005). The second category includes landslides in which the ~~the~~ upper layer containing hard rock (such as granite and sandstone) has a crushing effect on the lower weak rock layer, causing the lateral expansion of the rock mass, resulting in a landslide (Cruden and Varnes, 1996; Emelyanova, 1986).

With respect to the theoretical study on rainfall-induced translational landslide, scholars and researchers worldwide have used physical simulation experiments, gemechanical model analysis, and satellite remote-sensing methods to investigate the genetic mechanism, initiation criteria, and sensitivity analysis of the safety factors. Fan et al. (2008) reproduced the deformation and failure process of the landslides via a physical simulation, and further verified the formation mechanism as well as the initiation criterion formula of the flat-push landslide previously studied by Zhang et al. (1994). Sergio et al. (2006) investigated the influence of the pore-water pressure on the stability of the rainfall-induced landslides, as well as the soil failure mode based on pore-water pressure via simulation experiments. Floris and Bozzano (2008) and Teixeira et al. (2015) obtained rainfall data based on the historical periodic rainfall conditions, and used physical experiments to establish an optimization model for rainfall-induced landslide initiation criteria for landslides in the southern Apennines and shallow landslides in northern Portugal; they also evaluated the landslide susceptibility and safety factors to evaluate the possibility of landslide reactivation induced by rainstorms. Barlow et al. (2003), and Martin and Franklin (2005) used the US land satellite ~~called~~

68 ~~enhanced thematic mapper~~ (ETM+) and the digital elevation model (DEM) ~~data~~ to detect the
69 residues of translational bedrock landslides in an alpine terrain. Bellanova et al. (2018) used
70 resistivity imaging to investigate the Montaguto translational landslide that occurred in the
71 southern part of the Apennines; they also established a refined geometric model to observe the
72 lithologic boundaries, structural features, and lateral and longitudinal discontinuities associated
73 with the sliding surfaces.

74 Scholars have conducted further research on the formation characteristics and genetic
75 mechanism of translational landslides by analyzing the previous studies that have collated and
76 analyzed the current research status of translational landslides. Based on the results of the previous
77 conducted studies, this study mainly focuses on the following two aspects.

78 (1) The occurrence of plate-shaped translational landslides is often unexpected and covert.
79 The plate-shaped translational landslides are primarily induced by rainfall; such events often occur
80 in the red-bed zone of the Qinba–Longnan mountainous area. Because of the dense population and
81 infrastructure observed in this area, the plate-shaped landslides, characterized by large volumes of
82 mass, and covert and abrupt occurrence, often cause massive property loss and casualties. During
83 the previous field investigation, such destructive events are often classified as small-scale bedrcok
84 collapses, instead of focusing on the hidden dangers associated with landslides.

85 (2) The field investigation and monitoring data for this type of landslide are often unavailable.
86 In previously conducted studies, specific geomechanical and physical models have been
87 established based on the historical rainfall records, and physical experiments have been conducted
88 in the laboratory to verify the failure model (Xu et al. 2006; Fan et al., 2008). However, long-term
89 on-site monitoring data and related analysis except the remote observation based on synthetic

aperture radar (SAR) or satellite for such landslides, have not been presented in previous studies. Therefore, several key field monitoring parameters, including the width of the crown crack, real-time rainfall, pore-water pressure, and groundwater level, should be evaluated to investigate and validate the deformation as well as failure mode of the translational landslides, and utilized to establish a geomechanical model.

Based on the formation mechanism of the translational landslide that has been established previously, we selected a typical and specific translational landslide (the Wobaoshi landslide) occurring in the Ba river basin of the Qinba–Longnan mountainous area, and conducted field investigation, long-term monitoring (February 2015 to July 2018), geomechanical model analysis, and numerical simulation to investigate the instability conditions and variation failure modes of this translational landslide under the influence of periodic rainfalls.

# 1. ~~Engineering Geology~~ Characteristics of the Wobaoshi Landslide

## 1.1. Landslide Location

The Wobaoshi landslide is located in the Ba river basin in the Qinba–Longnan mountainous area. Its specific location is in Baiyanwan village, Sanhui town, Enyang district in Bazhong, China. Fig. 1 presents the geographical location and elevation information. The Wobaoshi landslide occurred on the left bank of the Shilong river. The front edge of this landslide is in the curved section of the river, whereas its left boundary gully was observed on the concave bank on the river's left bank. The landslide area is classified as a red-bed layer in the low mountainous area, the vegetation of its main body is dense, and its geomorphic unit is cuesta structural slope. The geologic structure of the body lies toward the south side of the Nanyangchang anticline, and the landslide involved sandstone and mudstone belonging to the Penglaizhen Formation of the upper

Jurassic series (Chen et al., 2015).

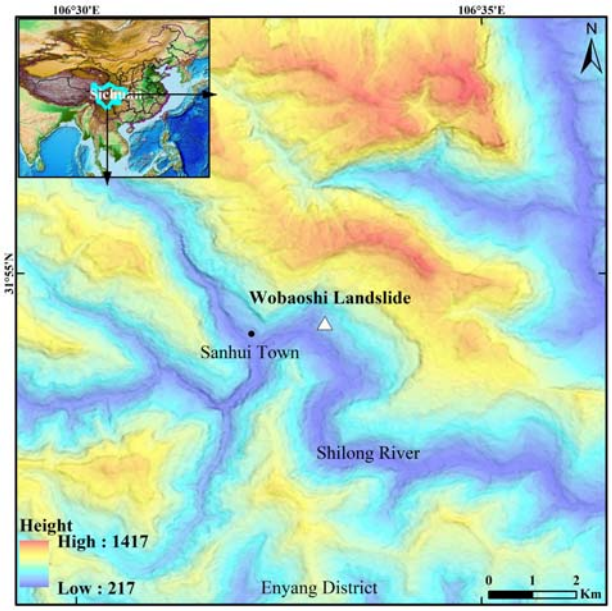


Fig. 1 Geographic location and elevation map of the Wobaoshi landslide.

This landslide occurred in the eastern subtropical monsoon climate region, where rainfall is abundant and mostly concentrated between May and October, accounting for 75% - 85% of the total annual rainfall. The monthly average rainfall is greater than 100 mm, the largest amount of rainfall occurs in July, which has a monthly average rainfall of more than 200 mm. Further, rainstorms can be frequently observed during July, and the rainfall in this region gradually decreases after August (Chen et al., 2015). The types of groundwater are mainly fissure water in weathered bedrock and pore-water in the cracks, and the dynamic change of groundwater is considerably affected by climatic change.

## 1.2. Landslide Characteristics ~~and Formation Conditions~~

~~1.2.1 Geometric Characteristics~~

The main body has a flat long rectangular shape on the plane according to the satellite remote sensing data and landslide survey. Its longitudinal (sliding) direction is nearly 32 m, lateral length is 160 m, the average thickness of the sliding body is approximately 30 m, and its volume is approximately $1.536 \times 10^5$ $m^3$ (Chen et al., 2015). This main body belongs to small- to medium-sized landslides according to the typical scale (Ministry of Land and Resources of the PRC; 2006). The sliding direction of the landslide is 249°, and the inclination degree of the rockbed is 6° ~ 8°. The strike in this landslide is almost parallel to the overall trend of the bank

slope, which is a gently inclined bedding rock ~~landslide.~~ Fig. 2 presents the schematic map of the Wobaoshi landslide and photographs of five observation points. Fig. 3 presents the I-I′ cross section ~~graph~~ of the landslide.

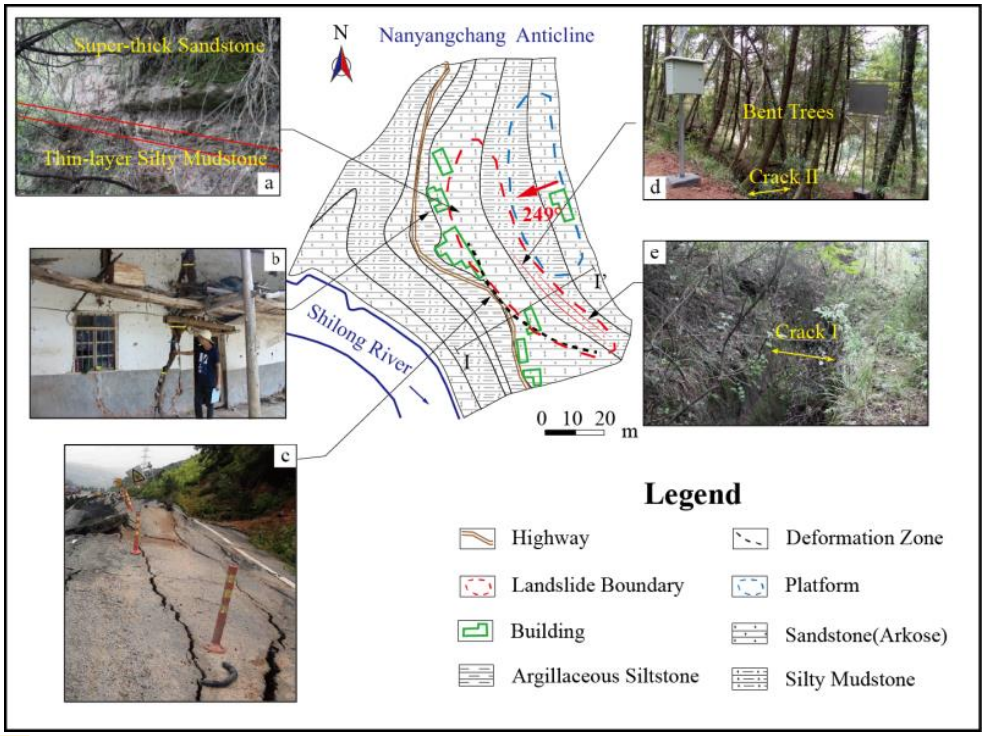


Fig. 2 The schematic map of the Wobaoshi landslide and photographs of the observation points: (a) exposed bedrock at the front edge; (b) the houses had cracked at the front edge (c) the roadbed is uplifted at the front edge; (d) crack II and bent trees; and (e) crack I.

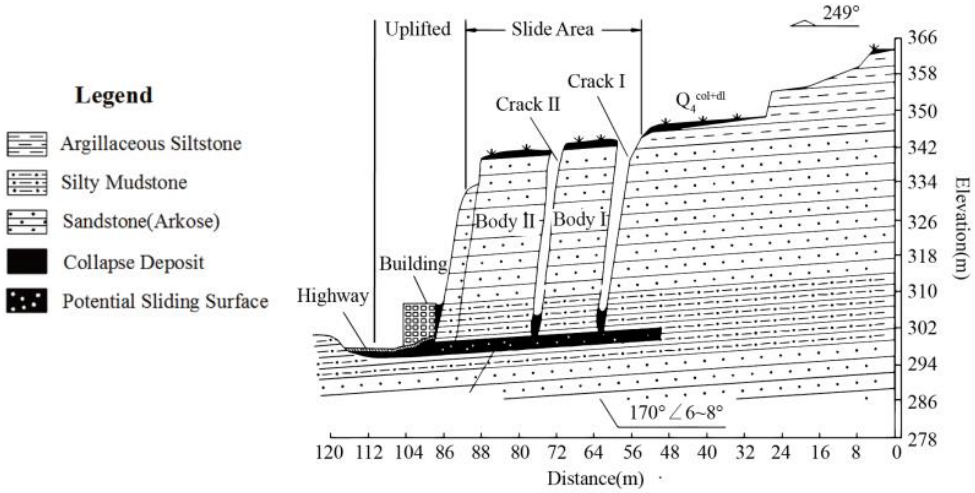


Fig. 3 The I-I′ cross section ~~graph~~ of the landslide

As shown in Fig. 2, the landslide is in a flat shape integrally, and its lengthwise is considerably smaller than the crosswise on the plane, and even smaller than the thickness of the

main body. Therefore, this body can be easily mistaken for a bedrock collapse during investigation of geological hazard. According to Fig. 3, the main bodies are almost perpendicular to the potential sliding surface, and a group of long and straight structural planes located parallel to the slope cut the slope into two narrow plates (bodies I and II); furthermore, the ~~structural~~ surface of the main body contain cracks, both sides of the crack are closed, and the bottom of the crack is filled with clay, gravel and collapse debris (Chen et al., 2015).

~~1.2.2 Conditions of the main bodies~~

The main body of the Wobaoshi landslide resulted in the formation of two main cracks from the outside to the inside, which cut and disintegrated the main body into plate-shaped blocks from front to back, as shown in the photographs of the observation points c and d in Fig. 2. The plate-shaped bodies I and II are aslo presented in Fig. 2. The landslide is a two-stage translational landslide in which the longitudinal length of body I is 12 m, the identifiable lateral width and thickness of which are approximately 70 and 30 m, respectively, and the longitudinal length of body II is 16 m, the identifiable lateral width and thickness of which are approximately 65 and 28 m, respectively. Body I forms crack I with the crown of the landslide, whereas body II forms crack II with body I. When large-intensity rainfall occurs during monsoon, pore-water can be observed in the cracks, indicating that cracks I and II exhibit preferable water-storage conditions.

As denoted by the photograph of the observation point d in Fig. 2 shows, bent trees grow on the crown of the landslide bodies I and II. The trees on the landslide are skewed with the sliding of the soil mass, after the sliding stops, the upper part of the trunk becomes more upright with each passing year. The existence of bent trees represents the tendency of the slope body to become unstable or that the existing landslide accumulation body may slide again, this is also historical evidence of the slow sliding movement of landslides (Zhang et al., 2015).

~~As denoted by the photo of the observation point a in Fig. 2,~~ the shallow surface of the Wobaoshi landslide is a 2–3 m thick layer comprising collapsed and plowed soil. The main body contains ~~extremely~~ thick sandstone with good integrity, whereas the bottom sliding surface is a weak interlayer ~~comprising~~ of silty mudstone. Thus, the Wobaoshi landslide is a typical and special translational landslide, it can be considered to be a plate-shaped landslide ~~based on the characteristics of its plate-shaped body~~ (Fan et al., 2008; Xu and Zeng, 2009; Xu et al., 2010).

The engineering geologic conditions of the Wobaoshi landslide can be observed based on its characteristics, i.e., the rapid immersion of groundwater softens the joint surface of soil and rock formation, especially under a rainstorm. Then, the group of open cracks located parallel to the slope in the main body is ~~concentrated and quickly~~ filled with water; subsequently, the groundwater level rises and the pore-water pressure increases drastically, such that bodies I and II will slide along the contact surface of the bottom sand-mud-rock weak layer. This condition changes the stress mode and equilibrium state of the rock and soil mass, easily inducing a landslide. ~~As can be observed at the observation point b and c in Fig. 2,~~ the Wobaoshi landslide pose a major threat to residential houses and highways, the houses cracked, and the highways were uplifted on its front edge, therefore, this landslide considerably threatens the safety of people's property and transportation.

## 2. Landslide Monitoring Scheme and ~~Monitoring~~ Data Analysis

### ~~2.1. Long-term Monitoring Scheme~~

According to the detailed investigation of the Wobaoshi landslide, two cracks are observed to extend through the sliding surface at the crown of the landslide. As the hydrostatic pressure in the cracks strongly influences the stability of the plate-shaped landslide (Fan et al., 2008; Guo et al., 2013), ~~via~~ real-time monitoring of cracks, rainfall and pore-water pressure measurements were conducted from February 2015 to July 2018 to determine the state of landslide during different periods such as rainy and non-rainy seasons, together with the interaction between multistage main bodies and the sliding surface. ~~Fig. 4 shows the layout graph of the monitoring equipment.~~

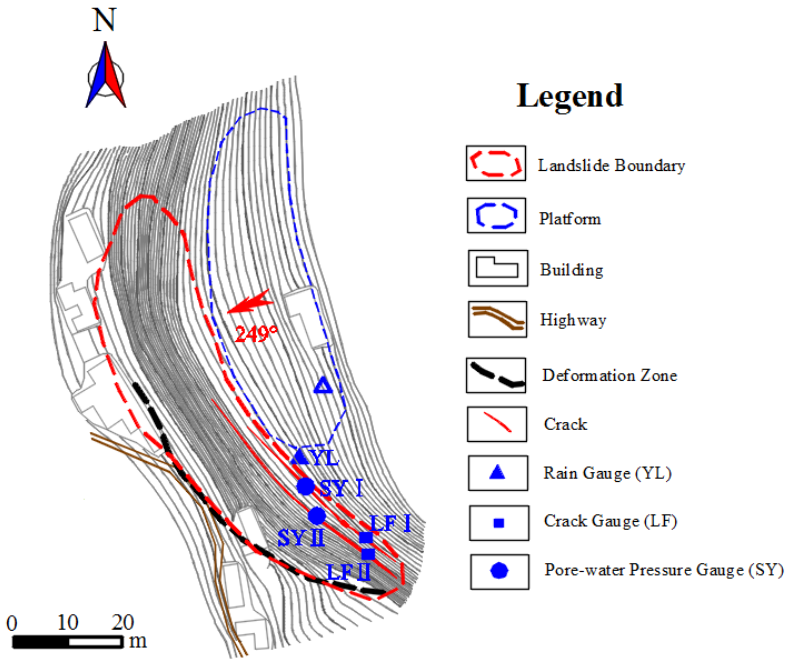


Fig. 4 Layout planar graph of the monitoring equipment

As shown in Fig. 4, two non-contact crack automatic monitors, LF I and II, are installed on both sides of cracks I and II, ~~respectively,~~ to record the real-time variation of the width with respect to the two cracks (Liu et al., 2015). An automatic rain gauge is installed in a flat space and no tree occlusion is observed at the crown of the landslide to record real-time and cumulative rainfall values. Two pore-water pressure gauges are installed at the bottom of cracks I and II to measure the pore-water pressure. The pore-water level, $h_c$, can be calculated using $h_c = H - h_i + h_m$, where *hi* is the installation depth of the pore-water pressure gauge, $H$ is the depth of the crack, and $h_m$ is the measured the pore-water pressure gauge.

In this example, the initial width of crack I is 5.640 m, whereas the initial width of crack II is 4.492 m (the first measurement was conducted in January 2015); the installation depth $h_{i1}$ = 24.72 m, and the depth of crack I is $H_1$ = 38 m, with $h_{c1}$ = 13.28m + $h_{m1}$. Additionally, the installation depth $h_{i2}$ = 24.85 m, the depth of crack I is $H_2$ = 35 m, and $h_{c2}$ = 10.15m + $h_{m2}$. The monitoring frequency of the crack width is thrice a day, the monitoring frequency of the pore-water pressure is twice a day, and the accumulative value for one month is considered to be the amount of rainfall. The multiparameter monitoring data are transmitted to the monitoring server through the GPRS network.

(a) (b) (c)

Fig. 5 Installation of the monitoring instrument: (a) crack I gauge; (b) rain gauge and pore-water pressure gauge; (c) crack II gauge.

## 2.2. Monitoring Data Analysis

~~In this study, we selected the typical data of the width of cracks I and II, the pore-water pressure and the amount of rainfall based on~~ the monitoring work conducted with respect to the Wobaoshi landslide for three-and-a-half years (February 2015 to July 2018); the details of these monitoring data are in presented in Tables 1 and 2. The ~~corresponding~~ time curves in Fig. 6 denote the monitoring data with respect to the amount of rainfall and the width of cracks I and II. Figs. 7(a) and 7(b) present the comparison curves of the monitoring data based on the width of cracks I and II with respect to their pore-water pressures, respectively.

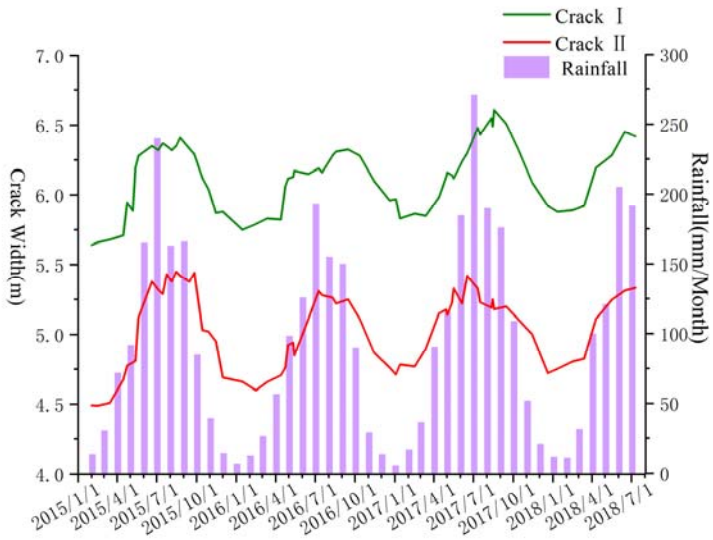

Fig. 6 The monitoring data curves (amount of rainfall and width of cracks I and II)

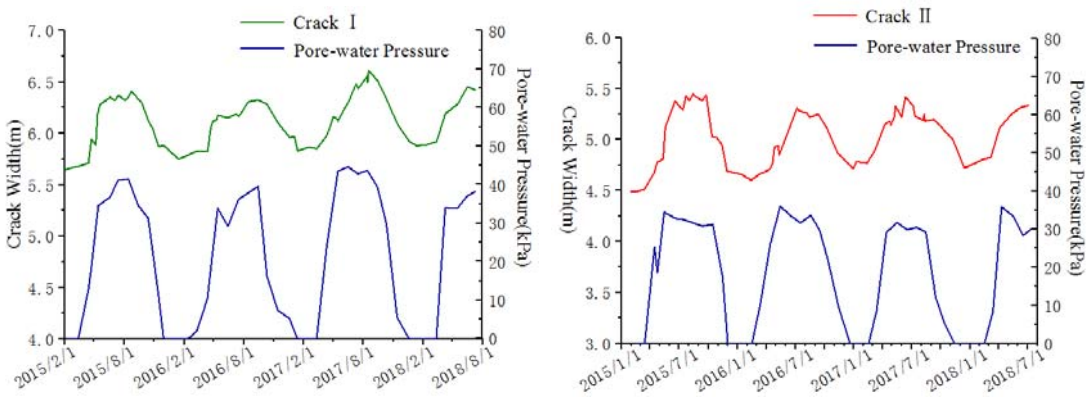


(a) (b)

Fig. 7 The monitoring data curves: (a) width of crack I and its pore-water pressure; (b) width of crack II and its pore-water pressure.

Based on the ~~comprehensive~~ comparison and analysis of the data curves in Figs. 6 and 7, the Wobaoshi landslide is still considered to be in the creep deformation state, and the plate-shaped body exhibits a regular trend with respect to the changes in amount of rainfall and pore-water pressure. Cracks I and II show a preferable water-storage capacity during monsoon, and the crack width variation is affected by the increasing pore-water pressure. The specific analysis can be given as follows.

(1) A clear correspondence can be observed between the absolute extension value of the crack width and season variation (i.e. ~~change in~~ amount of rainfall); the ~~magnitude of~~ amount of rainfall can be used to determine the variation of the width of the two cracks. As shown in Fig. 6, the widths of cracks I and II increase with an increase in the amount of rainfall during monsoon (May to September), whereas their crack widths gradually decrease ~~with decreasing the amount of rainfall~~ during the non-rainy seasons (October to April ~~in the next year~~). As indicated in Fig. 8, the

252 maximum width of crack I is 6.615 m, and its absolute extension value is approximately 1 m
253 during July ~ August in 2017 (during which the monthly rainfall is greater than 250 mm). The
254 maximum width of crack II is 5.40 ~ 5.45 m, and its absolute extension value is also
255 approximately 1 m during July ~ August in 2015 and 2017. During the non-rainy seasons, when
256 the amount of rainfall decreases, the crack width decreases and the minimum value can be
257 observed in January of each monitored year.

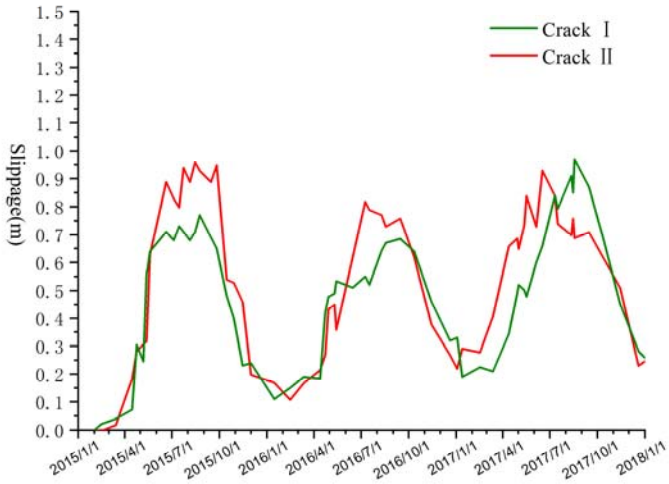


258

259 Fig. 8 The curves of the absolute extension value of crack I and II

260

261 (2) The width of cracks I and II tend to increase year by year, indicating that the two-stage
262 body of the Wobaoshi landslide is still moving owing to the influence of rainfall. In Fig. 6, the
263 data obtained during the monitoring period indicate that the minimum widths of crack I and II
264 gradually increase and that, their ~~maximum~~ value is considerably affected by the amount of
265 rainfall ~~during a particular month~~.

266 (3) Fig. 7 shows that the stretching of cracks I and II, or of both the curves follows the same

trend as the pore-water pressure, i.e., the magnitude of pore-water pressure determines the width variation of the cracks. Fig. 7(a) shows that crack I exhibits good water-storage during monsoon, after the main body slides, a certain pore-water level can be maintained because of rainfall. Additionally, the increase in amount of rainfall increases the water level in the cracks, and the increase in pore-water pressure positively affects the initiation of the main bodies. The curves in Fig. 7 denote that the increase in pore-water pressure has a significant causal relation with the stretching of the cracks.

# 3. Model Calculation and Numerical Simulation

A geomechanical model of plate-shaped bodies was established to obtain a ~~generic~~ model with respect to the evolution process ~~in case~~ of the Wobaoshi landslide; further, its stability was estimated, and it was used ~~along~~ with the monitoring data for performing comparative analysis. According to previous studies (Fan, 2007; Fan et al., 2008; Xu et al., 2010), the water pressure on both sides of each plate-shaped body attains a balanced state, except for the outermost body, when many penetrating cracks are located parallel to the slope in the rock mass and filled with water. However, once the outer body slides, the surrounding water pressure immediately following the plate-shaped body becomes unbalanced and new sliding ~~damage~~ is induced owing to the sudden decrease in the pore water level in the crown crack (Fan, 2007; Xu et al., 2010).

## 3.1. Model Establishment and Stability Calculation

According to the characteristics of the Wobaoshi landslide ~~presented in Section 1.2~~, the cover layer is neglected when establishing the geomechanical model, and a static geomechanical model of the plate-shaped rock body is established ~~on~~ using the limit equilibrium method. The basic characteristic of the limit equilibrium method is that the Mohr-Coulomb failure criterion of the soil under static equilibrium conditions is considered, i.e., the problem can be solved by analyzing

the destruction of the soil's balance (Vardoulakis, 1983). Further, the soli elastic-plastic ideal model, which obeys the Mohr-Coulomb failure criterion and the associated flow rules, is selected (Darve and Vardoulakis, 2004; Labuz and Zang, 2015).

In this study, we selected a typical section of plate-shaped bodies and established the geomechanical model, as shown in Fig. 9, with respect to the failure mode of the two-stage body of the Wobaoshi landslide. In this section, the outer layer body II is subjected to stability analysis; subsequently, the inner body I is analyzed.

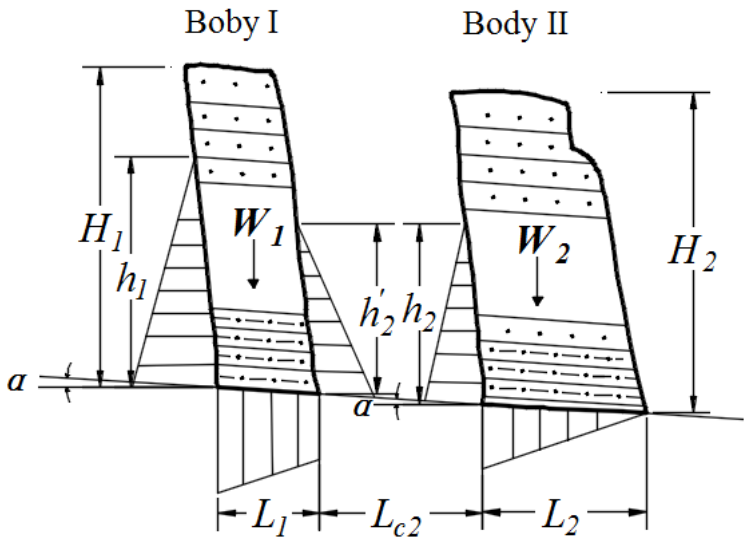


Fig. 9 Geomechanical model of the two-stage plate-shaped bodies

In Fig. 9, $\alpha$ denotes the angle of the sliding surface, $h_1$ and $h_2$ are the heights of the pore-water levels in cracks I and II, ~~respectively,~~ $L_1$ and $L_2$ are the widths of bodies I and II, ~~respectively,~~ $L_{c2}$ is the distance between bodies I and II; $H_1$ and $H_2$ are the heights of bodies I and II, ~~respectively,~~ and $W_1$ and $W_2$ are the self-weights of body I and II per unit ~~width, respectively.~~ According to the relation between the stability coefficient of the main body, $K$, and the height of the pore-water level, $h$, shown in Fig. 7 (Zhang et al., 1994; Xu et al., 2010), the stability coefficient, $K_2$ of the outer layer body II can be obtained as follows when considering the internal cohesive force of the sliding surface.

$$K_2 = \frac{\left(W_2 \cos\alpha - \frac{1}{2}\gamma_w h_2 L_2 - \frac{1}{2}\gamma_w h_2^2 \sin\alpha\right)\tan\theta + cL_2}{\frac{1}{2}\gamma_w h_2^2 \cos\alpha + W_2 \sin\alpha}. \quad (1)$$

Here, $c$ is the internal cohesion of the sliding surface; $\gamma_r$ is the unit weight of the saturated volume of sandstone; $\gamma_w$ is the unit weight of water; and $W = H{\cdot}L{\cdot}\gamma_r$. $K_2$ is set to 1, i.e., body II is set in a critical sliding state (GB/T 32864-2016, 2017). Eq. (2) is derived from Eq. (1) and can be used to calculate the maximum pore water level of body II $h_{cr2}$.

$$h_{cr2} \approx \frac{1}{2\cos\alpha}\left[L_2^2 \tan^2\theta + \frac{8}{\gamma_w}\left(W_2 \cos\alpha \tan\theta - W_2 \sin\alpha + cL_2\right)\cos\alpha\right]^{\frac{1}{2}} - \frac{L_2}{2\cos\alpha}\tan\theta \quad (2)$$

According to the experimental data obtained based on the triaxial test of the Wobaoshi landslide's rock core (Chen et al., 2015), the internal friction angle of the sliding surface is $\theta$ = 11.2°, the unit weigth of the saturated volume of the sandstone is $\gamma_r$ = 19.2 kN/m$^3$, the unit weight of clear water is $\gamma_w$ = 9.8 kN/m$^3$, and the internal cohesion of the sliding surface is $c$ = 10.2 kPa. According to the sectional graph of the Wobaoshi landslide (Fig. 2), $H$ = 35 m, $L$ = 16 m, and $\alpha$ = 6°. Therefore, according to Eq. (2), $h_{cr2}$ = 13.896 m.

Based on the stability analysis of body II, using Eq. (1) and (2), and Fig. 7, the stability coefficient $K_1$ of the inner layer body I can be obtained using Eq. (3). In addition, $h_2' = h_2 - L_{c2}\sin\alpha$ and $L_{c2}$ = 3.8 m; therefore, $h_2'$ = 13.499 m.

$$K_1 = \frac{\left[W_1 \cos\alpha - \frac{1}{2}\gamma_w\left(h_1 + h_2'\right)L_1 - \frac{1}{2}\gamma_w\left(h_1^2 - h_2'^2\right)\sin\alpha\right]\tan\theta + cL_1}{\frac{1}{2}\gamma_w\left(h_1^2 - h_2'^2\right)\cos\alpha + W_1 \sin\alpha} \quad (3)$$

Similarly, $K_1$ is set to 1; in body I, $H_1$ = 38m, $L_1$ = 12m, $\alpha$ = 6°, $h_2'$ = 13.499m, therefore, the

maximum pore-water level $h_{cr1}$ of body I can be calculated using the Eq. (3) and $h_{cr1}$ = 17.249m.

The preceding calculation results show that the pore water pressure triggers the plate-shaped bodies when the pore water level at the rear of the body reaches the maximum height at which the landslide begins, i.e., when $h_{cr1}$ = 17.249 m and $h_{cr2}$ = 13.896 m. In the next section, the pore water monitoring data, acquired via landslide monitoring, are used to verify Eq. (2) and (3).

The pore-water monitoring data presented in Section 2.2, acquired via long-term monitoring, were used to verify the equation applied to calculate the maximum height of the multistage bodies, ~~$h_{cr}$~~. According to the monitoring data obtained with respect to the pore-water pressure and installation depth of the sensors, the actual calculated maximum height values $h_{c1}$ and $h_{c2}$ of the pore-water level are presented in Table 3. Combined with the change in the absolute extension value in Fig. 8, the typical data with respect to the measured pore-water level are selected, corresponding to a sudden increase in absolute slippage (see Table 3 for details), as shown in Fig. 10.

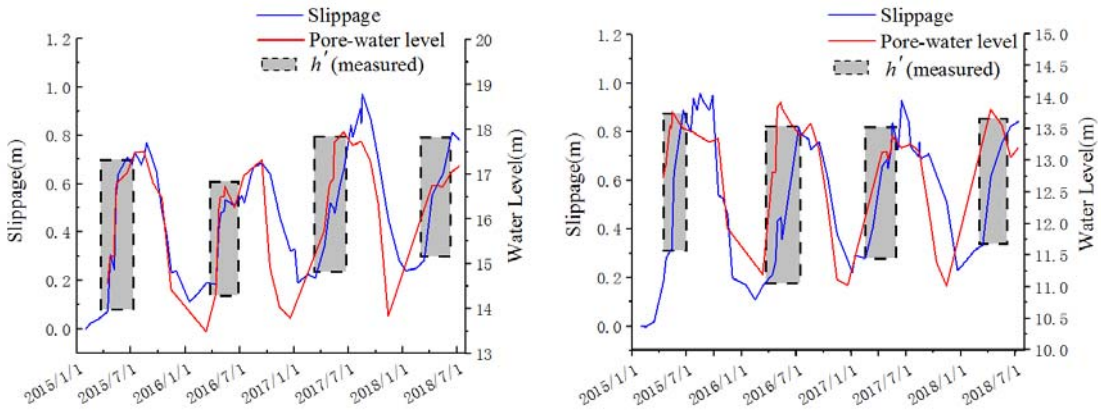


(a) Crack I (b) Crack II

Fig. 10 Determination of the maximum measured pore-water level $h_{cr}^{'}$

The dotted boxes in Fig. 10 denote the pore-water level when the bodies are sliding or tilting,

i.e., the maximum pore-water level, $h_{cr}^{'}$, which causes the main body to be unstable. The measured $h_{cr}^{'}$ in Fig. 10 can be compared with the relation between the pore-water level, $h$, and the stability coefficient of the body, $K$, obtained using Eqs. (1) and (3), respectively, which are also depicted in Fig. 11.

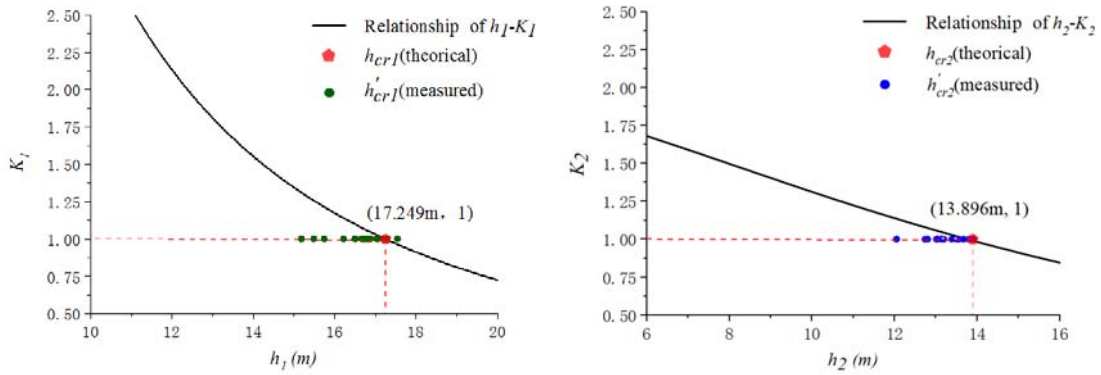


(a) Crack I (b) Crack II

Fig. 11 Comparison of $h_{cr}^{'}$(measured) and $h_{cr}$ (theoretical)

In Fig. 11, the curves of the h-k relation represent Eqs. (1) and (3). The values of $h_{cr}^{'}$ (measured) in Fig. 12 denote that majority of the monitoring pore-water levels are not higher than the theoretically calculated levels. The Wobaoshi landslide monitoring example shows that in majority of cases, the pore water pressure causes the main body to become unstable when $h_{cr}^{'}$ (measured) $\leqslant$ $h_{cr}$ (theoretical).

### 3.2. Numerical Simulation of the Plate-shaped Main Bodies

Numerical simulations and calculations were performed with respect to the main bodies using the MIDAS GTS NX geotechnical finite element software. First, the 1:1 main body model presented in Fig. 9 was introduced into the aforementioned software, and the mechanical parameters of the main body model, i.e., elastic modulus, Poisson's ratio, gravity internal cohesion and friction angle, were defined as shown in Table 4. The left and right boundaries were located at

a distance of approximately 30 m from bodies I and II respectively, and the lower boundary is observed to be located at sea level. A plane strain quadrilateral–triangle mixing element is considered, and the entire model is divided into 13775 elements and 14026 nodes. Here, we constrain the vertical and horizontal displacement of its bottom boundary, and the left and right boundary conditions are established to constrain the horizontal displacement. The model uses steady-state seepage calculation, and the water levels at the left and right boundaries were 342 and 275 m, respectively. The boundary conditions were set as follows.

(1) In case of the displacement boundary, the left and right boundaries constrained the displacement in the X-direction; i.e., TX = 0. In case of the bottom boundary, the displacements in the X and Y directions were constrained; i.e., TX = TY = 0.

(2) In case of the seepage conditions, the water levels at the left and right boundaries were set to 342 and 275 m, respectively.

The typical pore-water-level data of the four cycles obtained from 2015 to 2018 with respect to crack I and II (presented in Table 3 and Fig. 10) were introduced into the finite element model, and selected for a typical cycle change period presented in Table 5, followed by numerical calculations to obtain the typical deformation and displacement states of the plate-shaped bodies during the rainy and non-rainy seasons, as shown in Fig. 12.

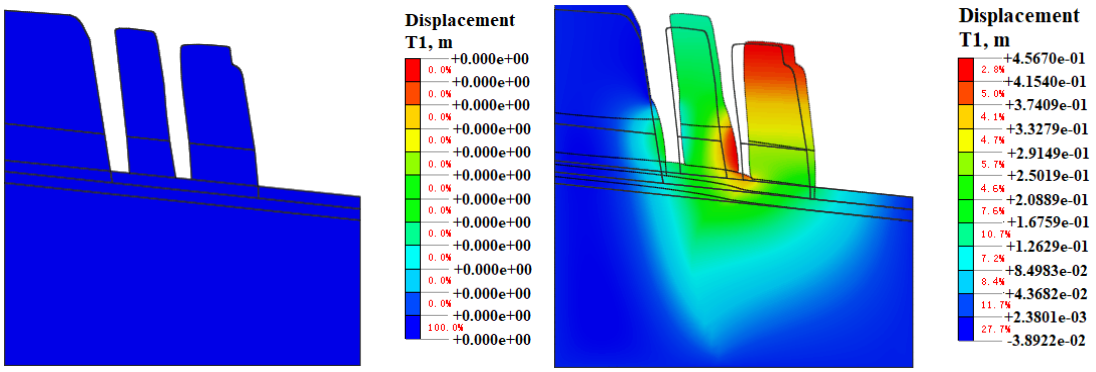


(a) The initial state (b) Tilt and slide occurs with an increase in pore-water level

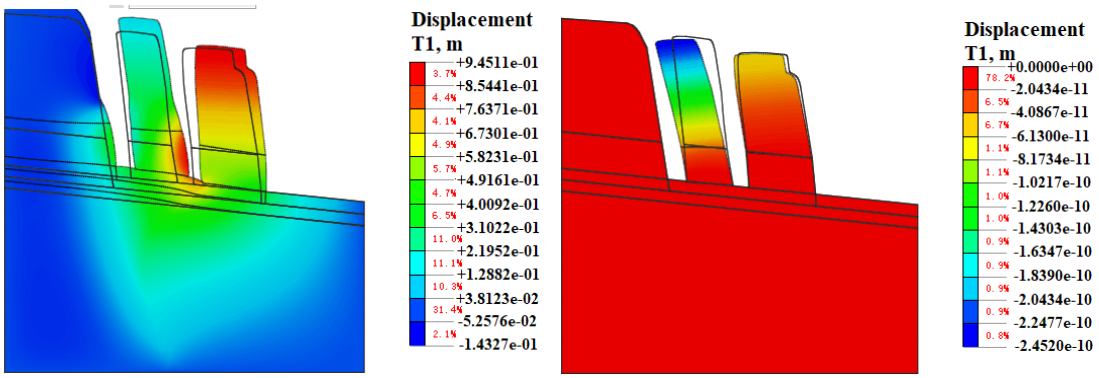


(c) The bodies slide to the maximum state (d) Bodies tilt backward when the water level decreases

Fig. 12 Example of finite element simulation and numerical calculation

The initial displacement state in Fig. 12(a) is set to zero for performing the following analysis. Fig 12(b) shows that, the multistage bodies deform horizontally along the sliding surface under the combined effect of pore water pressure and seepage. In Fig. 12(c), the multistage bodies have slid to the maximum distance, where the maximum distance of slider II is 0.945 m, which is approximately similar the value obtained in the monitoring data. In Fig. 12(d), bodies I and II exhibit the same tendency of tilting backward owing to the decrease in pore water level during the non-rainy season. Therefore, the calculation results obtained via the numerical simulations can corroborate the main body mechanics model and landslide monitoring data.

# 4. Discussion

The deformation or sliding movement of the nearly horizontal bedrock slope is almost impossible according to the traditional theory of granular equilibrium limit, and the likelihood of occurrence of a landslide is minimal. However, the special structure of translational landslide develops mainly in the Qinba–Longnan mountainous area when investigating geological hazards. Therefore, the characteristics of the plate-shaped landslide and the deformation and failure modes should be combined during the investigation and risk assessment of geological hazards to detect the hidden dangers associated with the geological conditions of the landslide. Based on the results obtained in previous studies and the monitoring results, the discussion presented in this study can

be divided into the following three parts.

### 4.1. Deformation and Failure Mode Analysis of the Wobaoshi Landslide

The monitoring results of the Wobaoshi landslide can be used to validate the rainfall-triggered failure mode of the translational landslide (Zhang et al., 1994). Based on the landslide monitoring data, particularly the change trend with respect to the opening and closing of the cracks presented in Section 2.2, and the numerical simulations of the plate-shaped bodies presented in Section 3.2, the deformation and failure modes were obtained with respect to the landslide, as shown in Fig. 13. Fig. 13 shows the deformation of the plate-shaped bodies of the Wobaoshi landslide during the monitoring period (non-rainy, season–rainy and season–non-rainy season). As shown in Fig. 13(b), the large amount of rainfall during monsoon causes the infiltration of cracks with water; when the pore-water level reaches the maximum height at which the landslide begins, the increased pore-water pressure positively affects the initiation of the plate-shaped body (Fan et al., 2007). The plate-shaped landslide can be triggered when the pore water pressure increases to the threshold value. In the monitoring case, the pore-water pressure can push the plate-shaped body by approximately 1 m, resulting in the uplift of residential houses and highways on its leading edge. Therefore, one or more penetrating cracks are likely to be parallel to the slope in the body. With the approach of the rainy season, the plate-shaped body II begins to slide firstly and the water-pressure balance in cracks is destabilized. This condition causes the gliding of the plate-shaped body I, forming a multistage translational landslide via characteristic step-by-step backward movements.

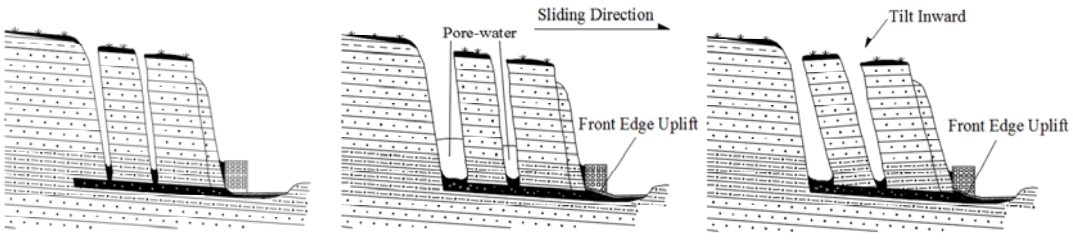


Fig. 14 Schematic of the deformation and failure mode of the Wobaoshi landslide

As shown in Fig. 13(c), the body is tilted to the crown of landslide because of the lower

pore-water level and its own weight when there is less rainfall during the non-rainy season, causing the body to fall backward (inside the slope) until the top of the body is in contact with the slope surface, the crack width begins shrinking, and a narrow A-shaped crack is formed. The monitoring data of the Wobaoshi landslide and numerical simulation of the plate-shaped body can be used to verify the deformation and failure mode of the plate-shaped landslide after its occurrence (Xu et al., 2010). With each passing year, the cracks at the bottom of the slab-shaped body increase in size, and the degree of inclination of the body also continues to increase. The degree of arching of the front edge also increases, causing the stability of the landslide to decrease continuously, posing a high risk for the houses and roads located toward the front edge of the landslide.

### 4.2. Determination of the Maximum Pore-water Level $h_{cr}$

The theoretical analysis and stability calculation of the geomechanical model of the body is described in Section 4.1, along with those of the initiation criterion for multistage main bodies in case of translational landslides, i.e., determination of the maximum water height in the crack, $h_{cr}$, (Zhang et al., 1994) and calculation of the body's stability coefficient, $K$, (Xu et al., 2010), which can be determined by theoretically calculating the strata inclination, shape, weight, and physical properties (unit weigth of the saturated volume, $\gamma_r$, internal cohesion of the sliding surface, $c$, and internal friction angle of the sliding surface, $\theta$) based on the limit equilibrium theory (Lin et al., 2010). Therefore, the stability coefficient of the landslide is observed to exponentially decrease with an increase in the water-filling height of the crown crack (Fan, 2008; Xu et al., 2010).

The internal friction angle, $\theta = 11.2°$, is considerably low for clay, and seems unrealistic. However, the angle $\theta$ is obtained via triaxial compression tests of the core, obtained from the sand-mudstone contact surface in the sliding surface, and the internal friction angle $\theta = 11.2°$ (Chen et al., 2015). This may be because the clay layer is severely weathered, resulting in a considerably small internal friction angle. Generally, the dilatancy effect obtained via the associated flow law is considerably larger than the actual observation, especially in the case of laternal confinement (Tschuchnigg et al., 2015a). However, in case of slope stability analysis, laternal infinite is mostly not considered, and the dilatancy effect is not significant (Griffiths &

458 Lane, 1999). Therefore, it is reasonable to set the dilatancy angle equal to the internal friction
459 angle.

460 In this case, with respect to the equation for calculating the maximum pore-water level, $h_{cr}$,
461 deduced in Section 3.1, we can observe that the measured maximum pore-water level, $h_{cr}^{'}$, is close
462 to the theoretical maximum pore-water level, $h_{cr}$, by comparing with the measured data obtained
463 in case of the Wobaoshi landslide in Section 2.2, validating the calculation equation of $h_{cr}$, and the
464 instability conditions of the main bodies. Additionally, the measured data in Table 3 are slightly
465 smaller than the theoretical calculation value, i.e., $h_{cr}^{'} \leq h_{cr}$. Thus, when compared with the
466 equation to calculate the maximum water height proposed by Zhang et al. (1994) and the physical
467 simulation experiment conducted by Fan et al. (2008), the monitoring case of the Wobaoshi
468 landslide shows that the $h_{cr}^{'}$ with respect to the measured data is mostly lower than the theoretical
469 calculated value, $h_{cr}$, which can destabilize the main body. This instability may be attributed to the
470 fact that the actual cohesion value $c'$ of the sand-shale contact surface is smaller than the cohesive
471 force value $c$ of the sliding surface in Eq. (2) during the creep state of the landslide for a long
472 duration or that the frictional angle of the sliding surface, $\theta$, changes slightly. According to the
473 calculation of the stability coefficient, $K$, in Eq. (2), when $c' \leq c$, $h_{cr}^{'} \leq h_{cr}$, the body slides when $h_{cr}^{'}$
474 (measured) is not larger than $h_{cr}$ (theoretical).

475 **4.3. Optimization Methods of Landslide Monitoring**

476 In this study, we propose a long-term monitoring method containing more parameters based
477 on the characteristics of the plate-shaped translational landslides by focusing on them in
478 accordance with the existing field-monitoring-result experience as well as deformation and failure
479 mode exploration.

480 First, long- term monitoring should be conducted to obtain sufficient monitoring data, ~~mainly~~
481 including ~~obtaining~~ the groundwater level, pore-water pressure, amount of rainfall, and
482 displacement data on the front edge of the landslide during monsoon, as well as focusing on the

change of the overall inclination of the body during the non-rainy season. This is because the inclination angle α relative to the sliding surface also changes after the body slides. Thus, an inclination measuring device, which comprises a three-axis accelerometer and electronic compass should be installed in the main body to verify the theoretical exploration of the deformation mode of the plate-shaped body during the non-rainy season in Fig. 13(c). Furthermore, a sensitivity analysis of the various parameters affecting the stability coefficient K of the main body (including the pore-water level, internal cohesive force in saturated water, internal friction angle of the sliding surface, and inclination angle of the body), should be conducted based on the monitoring data. Therefore, a detailed analysis and exploration of the deformation and failure mode of the plate-shaped landslide would be beneficial and improve the success rate of landslide warning.

## 5. Conclusions

By considering Wobaoshi landslide as an example, we use research methods, including field exploration, long-term monitoring engineering, geomechanical model analysis, and numerical simulation, to analyze the instability conditions and failure characteristics of a special type of translational landslide. The obtained research results are beneficial with respect to the stability analysis and evaluation of this type of landslide. Targeted monitoring methods are proposed to enrich theoretical research on translational landslides. The following conclusions can be obtained.

(1) The characteristics, formation conditions, and occurrence mechanism of the rainfall-triggered plate-shaped landslides are summarized in this study. Such landslides can be generally observed in a consequent slope where the inclination angle of the sliding surface is observed to be less than 10°, and a group of long and straight structural planes observed parallel to

505 the slope cuts the slope into several narrow plates. The plate-shaped body generally contains
506 extremely thick sandstone, which is nearly horizontal and exhibits good integrity. The bottom
507 sliding zone is a weak mudstone interlayer that is affected by the periodic rainfalls. In addition,
508 single or multistage plate-shaped bodies slide horizontally along the bottom mudstone sliding
509 zone.

510 (2) The relation between the stability coefficient of the multistage body $K$ and the pore water
511 level $h$ was obtained based on the mechanical model of the plate-shaped bodies, and the maximum
512 pore water level $h_{cr}$, which causes the instability of the multistage bodies, was calculated. The
513 instability conditions of the plate-shaped bodies were also determined.

514 (3) The theoretical conclusions of the plate-shaped landslide research were verified based on
515 the long-term monitoring data. The multiparameter monitoring data denote that the stability of the
516 main body is considerably affected by the rainfall intensity and pore water pressure. The pore
517 water pressure in the crack is positive at the beginning of the plate-shaped body, demonstrating the
518 rainfall-triggered failure mode of the translational landslide. In this study, we compare and analyze
519 the measured maximum pore water level $h_{cr}^{'}$ as well as the theoretical calculated value $h_{cr}$ and
520 discuss the influence of the variation of the internal cohesive force and internal friction angle on
521 the stability coefficient of the main body.

522 (4) Based on landslide numerical simulation, we analyze and explore the deformation and
523 failure modes of the plate-shaped landslide, i.e., the main bodies are considered to slide
524 horizontally along the contact surface of the bottom sand–mud–rock weak layer based on the pore
525 water pressure in the crack and the seepage effect during monsoon. During the non-rainy season,

526 the pore water pressure decreases and disappears; the main body will be inclined to the crown of
527 the landslide owing to its dead weight. Thus, in this study, we propose an optimized monitoring
528 methodology to closely monitor the pore water pressure, rainfall, and landslide frontal
529 displacement during monsoon; the proposed method focuses on the overall inclination angle
530 variation of the body during the non-rainy season.

531

## 532 Acknowledgments

533 We thank Dr. Long Chen at the Institute of Exploration Technology of CAGS for providing
534 landslide monitoring data. This work was supported by the National Natural Science Foundation
535 of China (41804089), Project of Observation Instrument Development for Integrated Geophysical
536 Field of China Mainland (Y201802), and CGS of China Geological Survey Project
537 (1212011220169 and 12120113011100).

538

## 539 References

540 Barlow, J., Martin, Y., and Franklin, S. E.: Detecting translational landslide scars using segmentation of
541 Landsat ETM+ and DEM data in the northern Cascade Mountains, British Columbia,
542 Canadian Journal of Remote Sensing, 29(4):510-517, 2003.

543 Bellanova, J., Calamita, G., Giocoli, A., Luongo, R., and Piscitelli, S.: Electrical resistivity imaging for
544 the characterization of the Montaguto landslide(southern Italy), Engineering Geology,
545 243(1):272-281, 2018.

546 Brown, E., and Hoek, E.: Trends in relationships between measured in-situ stresses and depth.
547 International Journal of Rock Mechanics and Mining Sciences & Geomechanics Abstracts,
548 15(4):78-85, 1978.

549 Chen, L., Liu, Y., and Feng, X.: The investigation report of Wobaoshi landslide, Sanhui Town, Enyang
550 District, Bazhong City, The Institute of Exploration Technology of CAGS, Chengdu, Open
551 File Rep., 57-75, 2015.

552 Cruden, D.M., and Varnes, D.J.: Landslide Types and Processes, Special Report , Transportation
553 Research Board, National Academy of Sciences, 247:36-75, 1996.

554 Darve, F., and Vardoulakis, I.: Degradations and Instabilities in Geomaterials, Springer Vienna, Austria,
555 2004.

556 Emelyanova, E.II.: The basic rule of landslide movement, Chongqing Publishing House, Chongqing,
557 China, 1986.

558 Fan, X., Xu, Q., Zhang, Z., Meng, D and Tang, R.: The genetic mechanism of a translational landslide,
559 Bulletin of Engineering Geology and the Environment, 68(2):231-244, 2009.

560 Fan, X.: Mechanism and remediation measures for translational landslide [M. S. Thesis], Chengdu:
561 Chengdu University of Technology, 2007.

562 Fan X., Xu Q., Zhang Z., Meng, D and Tang, R.: Study of genetic mechanism of translational landslide,
563 Chinese Journal of Rock Mechanics and Engineering, 27(Supp.2):3753-3759, 2008.

564 Floris, M., Bozzano, F.: Evaluation of landslide reactivation: a modified rainfall threshold model based
565 on historical records of rainfall and landslides, Geomorphology, 94(1-2): 40-57, 2008.

566 Griffiths, D. V., and Lane, P. A.: Slope stability analysis by finite elements, Géotechnique, 49(3),
567 387-403, 1999.

568 Guzzetti, F., Cardinali, M., Reichenbach, P., and Francesco, C.: Landslides triggered by the 23
569 November 2000 rainfall event in the Imperia Province, Western Liguria, Italy, Engineering
570 Geology, 73(3-4):229-245, 2004.

571 Guo, X., Huang, R., Deng, H., Xu, Q., and Zhai, G.: Formation and mechanism analysis of multi-level
572 rift trough in translational sliding landslide, Journal of Engineering Geology, 21(5):770-778,
573 2013.

574 Kong, J., and Chen, Z.: The translational landslide in red stratum located in east of Sichuan in July,
575 1989. Beijing: China Railway Publishing House, Landslide Column(9), 1989.

576 Labuz, J. F., and Zang, A.: Mohr–Coulomb Failure Criterion, Rock Mechanics and Rock Engineering,
577 (2012)45:975–979, 2012.

578 Lin, J., Yang, W., and Bao, C.: Progressive collapse mechanism of hybrid structures with different
579 vertical stiffness, China Earthquake Engineering Journal, 40(4):713-720, 2018.

580 Liu, Y., and Wang, J.: The research and application of landslide surface crack monitoring method based
581 on laser ranging mode, Environmental and Earth Sciences Research Journal, 2(2):19-24, 2015.

582 Martin, Y. E., and Franklin, S. E.: Classification of soil- and bedrock-dominated landslides in British
583 Columbia using segmentation of satellite imagery and DEM data, International Journal of
584 Remote Sensing, 26(7):1505-1509, 2005.

585 Matjaž, M., Matja, C., and Mitja, B.: Hydrologic conditions responsible for triggering the Stože

586 landslide, Slovenia, Engineering Geology, 73(3-4):193-213, 2004.

587 Ministry of Land and Resources of the PRC: Specification of Design and Construction for Landslide
588 Stabilization (DZ/T 0219-2006), 2006.

589 Sergio, D. N., Lourenco, K. S., and Hiroshi, F.: Failure process and hydrologic response of a two layer
590 physical model: Implications for rainfall-induced landslides, Geomorphology, 73(1-2):115-130,
591 2006.

592 Teixeira, M., Bateira, C., and Marques, F.: Physically based shallow translational landslide
593 susceptibility analysis in Tibo catchment, NW of Portugal, Landslides, 12(3):455-468, 2015.

594 Tschuchnigg, F., Schweiger, H.F. and Sloan, S.W.: Slope stability analysis by means of finite element
595 limit analysis and finite element strength reduction techniques. Part I: Numerical studies
596 considering non-associated plasticity, Computers and Geotechnics, 70, 169-177, 2015.

597 Tschuchnigg, F., Schweiger, H.F., and Sloan, S.W.: Comparison of finite-element limit analysis and
598 strength reduction techniques, Géotechnique, 65(4), 249-257, 2015.

599 Wang, L.，and Zhang, Z.: The mechanical patterns of the deformation in rock slope, Geological
600 Publishing House, Beijing, China, 1985.

601 Vardoulakis, I.: Rigid granular plasticity model and bifurcation in the triaxial test, Acta Mechanica,
602 49(1):57-79, 1983.

603 Xu, Q., and Zeng, Y.: Research on acceleration variation characteristics of creep landslide and
604 early-warning prediction indicator of critical sliding, Chinese Journal of Rock Mechanics and
605 Engineering, 28(6):1099-1106, 2009.

606 Xu, Q., Huang, R., and Liu, T..: Study on the formation mechanism and design of control engineering
607 for the super-huge Tiantai landslide, Xuanhan County, Sichuan Province, China, IAEG2006
608 Engineering Geology for Tomorrow Cities, Sichuan province, China, 2006.

609 Xu, Q., Fan, X., Li, Y., and Zhang, S.: Formation condition, genetic mechanism and treatment measures
610 of plate-shaped landslide, Chinese Journal of Rock Mechanics and Engineering,
611 29(2):242-250, 2010.

612 Yin, K., Jian, W., and Zhou, C.: Study on the mechanism of the translational landslide in Wanzhou
613 district and prevention project, Wuhan: China University of Geosciences，Open File,
614 pp.153-154, 2005.

615 Zhang, L., Pei, X., Lin, H., and Li, S.: Evolution of Landslide Based on Growth Characteristics of
616 Trees on the Landslide, Mountain Research, 33(4):503-510, 2015.

617 Zhang, Z., Wang, S., and Wang, L.: The analytical principle on engineering geology, Geological
618 Publishing House, Beijing, China, 1994.

## Figure Captions

Fig. 1 Geographic location and elevation map of the Wobaoshi landslide.

Fig. 2 Schematic map of the Wobaoshi landslide and photographs of the observation points: (a) exposed bedrock at the front edge; (b) the houses were cracked at the front edge (c) the roadbed is uplifted at the front edge; (d) crack II and bent trees; and (e) crack I.

Fig. 3 I- I′ cross-section graph of the landslide.

Fig. 4 Layout planar graph of the monitoring equipment.

Fig. 5 installation of the monitoring instruments: (a) crack I gauge; (b) rain gauge and pore-water pressure gauge; and (c) crack II gauge.

Fig. 6 The monitoring data curves (amount of rainfall and width of cracks I and II).

Fig. 7. The monitoring data curves: (a) width of crack I and its pore-water pressure; (b) width of crack II and its pore-water pressure.

Fig. 8 The curves of the absolute extension value of crack I and II.

Fig. 9 Geomechanical model of the two-stage plate-shaped bodies.

Fig. 10 Determination of the maximum measured pore-water level $h_{cr}^{'}$.

Fig. 11 Comparison figure of $h_{cr}^{'}$ (measured) and $h_{cr}$ (theoretical).

Fig. 12 Example of finite element simulation and numerical calculation.

Fig. 13 Schematic of the deformation and failure mode of the Wobaoshi landslide.

## Table

Table 1 Typical monitoring data in case of the Wobaoshi landslide

| Measurement duration | Crack I width (m) | Crack II width (m) | Crack I Pore-water pressure (kPa) | Crack II Pore-water pressure (kPa) |
|---|---|---|---|---|
| 2015/2/1 | 5.640 | 4.492 | 0 | 0 |
| 2015/4/24 | 5.945 | 4.774 | 18.561 | 27.303 |
| 2015/5/7 | 5.886 | 4.798 | 18.649 | 33.212 |
| 2015/5/13 | 6.203 | 4.810 | 33.134 | 33.036 |
| 2015/5/15 | 6.215 | 4.899 | 34.476 | 35.456 |
| 2015/8/15 | 6.350 | 5.451 | 41.474 | 31.625 |
| 2015/9/14 | 6.330 | 5.380 | 34.594 | 30.772 |
| 2015/11/15 | 5.871 | 4.952 | 11.280 | 17.395 |
| 2016/2/15 | 5.790 | 4.599 | 0 | 0 |
| 2016/4/13 | 5.824 | 4.706 | 10.378 | 26.156 |
| 2016/5/14 | 6.173 | 4.850 | 33.810 | 36.035 |
| 2016/7/17 | 6.161 | 5.281 | 36.162 | 31.664 |
| 2016/8/18 | 6.310 | 5.220 | 38.024 | 33.683 |
| 2016/9/15 | 6.325 | 5.251 | 39.298 | 29.723 |
| 2016/12/20 | 5.960 | 4.763 | 5.106 | 0 |
| 2017/2/16 | 5.865 | 4.770 | 0 | 0 |
| 2017/4/13 | 5.984 | 5.152 | 24.108 | 29.155 |
| 2017/5/17 | 6.118 | 5.332 | 43.463 | 31.703 |
| 2017/7/17 | 6.433 | 5.239 | 42.787 | 30.478 |
| 2017/8/15 | 6.490 | 5.255 | 43.639 | 29.273 |
| 2017/11/14 | 6.091 | 5.004 | 5.488 | 8.428 |
| 2017/12/20 | 5.922 | 4.723 | 0 | 0 |
| 2018/1/11 | 5.881 | 4.751 | 0 | 0 |
| 2018/4/10 | 6.194 | 5.110 | 33.957 | 35.819 |
| 2018/5/17 | 6.283 | 5.246 | 33.830 | 33.438 |
| 2018/6/16 | 6.452 | 5.315 | 36.995 | 28.391 |
| 2018/7/10 | 6.421 | 5.310 | 38.171 | 29.841 |

Table 2 Amount of rainfall value of the Wobaoshi landslide (mm/month)

| Year \ Month | 1 | 2 | 3 | 4 | 5 | 6 | 7 | 8 | 9 | 10 | 11 | 12 | Total |
|---|---|---|---|---|---|---|---|---|---|---|---|---|---|
| 2015 | | 13.5 | 30.5 | 71.8 | 121.9 | 165.0 | 240.1 | 163.0 | 166.1 | 85.0 | 39.6 | 14.1 | 1110.6 |
| 2016 | 6.9 | 12.5 | 26.5 | 56.8 | 98.4 | 126.1 | 193.2 | 155.1 | 150.0 | 90.3 | 29.1 | 13.5 | 958.4 |
| 2017 | 5.7 | 16.8 | 36.8 | 90.5 | 115.6 | 185.1 | 271.3 | 190.0 | 176.2 | 109 | 52.1 | 20.8 | 1269.9 |
| 2018 | 11.5 | 10.9 | 31.5 | 99.9 | 121.0 | 205.1 | 191.6 | \ | \ | \ | \ | \ | 671.5 |

644 Table 3 The measured pore-water level data of the main bodies

| Measured time | Crack Ⅰ slippage (m) | Measured pore-water level (m) | Crack II slippage (m) | Measured pore-water level (m) |
|---|---|---|---|---|
| 2015/4/15 | 0.072 | 14.566 | 0.183 | 12.736 |
| 2015/4/24 | 0.305 | 15.174 | 0.282 | 12.936 |
| 2015/5/7 | 0.246 | 15.183 | 0.306 | 13.539 |
| 2015/5/13 | 0.561 | 16.661 | 0.318 | 13.521 |
| 2015/5/15 | 0.573 | 16.798 | 0.407 | 13.768 |
| 2015/6/20 | 0.711 | 17.032 | 0.888 | 13.502 |
| 2015/7/17 | 0.519 | 17.474 | 0.798 | 13.471 |
| 2015/10/16 | 0.481 | 16.470 | 0.538 | 13.340 |
| 2015/11/15 | 0.229 | 14.431 | 0.458 | 11.925 |
| 2016/1/15 | 0.108 | \ | 0.169 | \ |
| 2016/4/13 | 0.184 | 13.490 | 0.214 | 12.819 |
| 2016/4/23 | 0.421 | 14.339 | 0.269 | 12.804 |
| 2016/4/29 | 0.475 | 16.214 | 0.432 | 13.835 |
| 2016/5/11 | 0.469 | 16.494 | 0.449 | 13.920 |
| 2016/5/14 | 0.531 | 16.505 | 0.358 | 13.827 |
| 2016/6/15 | 0.508 | 16.731 | 0.618 | 13.574 |
| 2016/9/15 | 0.683 | 17.312 | 0.758 | 13.183 |
| 2016/10/12 | 0.637 | 14.930 | 0.618 | 12.360 |
| 2017/2/16 | 0.223 | \ | 0.278 | \ |
| 2017/4/13 | 0.344 | 15.741 | 0.658 | 13.125 |
| 2017/4/29 | 0.489 | 16.712 | 0.686 | 13.141 |
| 2017/5/2 | 0.518 | 16.799 | 0.648 | 13.024 |
| 2017/5/13 | 0.501 | 16.877 | 0.734 | 13.161 |
| 2017/5/17 | 0.476 | 17.715 | 0.838 | 13.385 |
| 2017/8/15 | 0.848 | 17.733 | 0.758 | 13.137 |
| 2017/9/16 | 0.869 | 16.324 | 0.333 | 12.235 |
| 2018/3/14 | 0.281 | \ | 0.618 | 11.013 |
| 2018/4/10 | 0.552 | 16.745 | 0.754 | 13.805 |
| 2018/5/17 | 0.643 | 16.732 | 0.333 | 13.562 |

645

646 Table 4 Mechanical parameters of the main body model

| Lithology | Elastic modulus ($N/m^2$) | Poisson ratio | Unit weigth (N) | Internal cohesion ($N/m^2$) | Internal friction Angle | Permeability coefficient (cm/s) |
|---|---|---|---|---|---|---|
| Arkose | 600000 | 0.25 | 19200 | 30000 | 36° | 1.20E-07 |
| Silty Mudstone | 360000 | 0.28 | 19000 | 20000 | 30° | 6.00E-07 |
| Clay | 300000 | 0.3 | 18000 | 10200 | 11.2° | 1.20E-06 |

647

648

649 Table 5 Loading steps of the water level in Crack I and II in FEM model

| Loading steps | Crack I | Crack II |
|---|---|---|
| 0 | 314.50 m | 311.00 m |
| 1 | 316.00 m | 313.00 m |
| 2 | 317.50 m | 315.00 m |
| 3 | 316.00 m | 313.00 m |
| 4 | 314.50 m | 311.00 m |

650